

Soft Matter

Accepted Manuscript

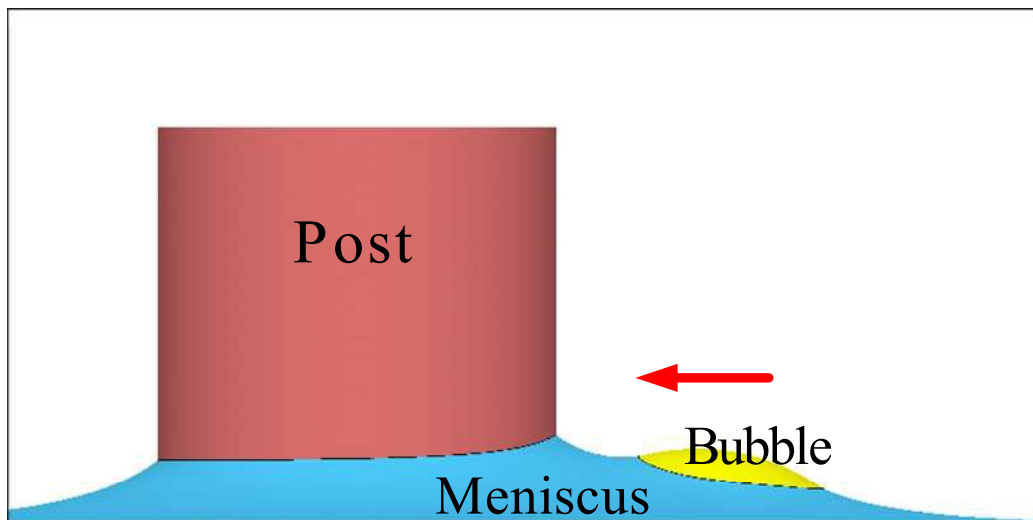


This is an *Accepted Manuscript*, which has been through the Royal Society of Chemistry peer review process and has been accepted for publication.

Accepted Manuscripts are published online shortly after acceptance, before technical editing, formatting and proof reading. Using this free service, authors can make their results available to the community, in citable form, before we publish the edited article. We will replace this *Accepted Manuscript* with the edited and formatted *Advance Article* as soon as it is available.

You can find more information about *Accepted Manuscripts* in the [Information for Authors](#).

Please note that technical editing may introduce minor changes to the text and/or graphics, which may alter content. The journal's standard [Terms & Conditions](#) and the [Ethical guidelines](#) still apply. In no event shall the Royal Society of Chemistry be held responsible for any errors or omissions in this *Accepted Manuscript* or any consequences arising from the use of any information it contains.



A bubble near a post-induced meniscus moves to the highest position of the triple contact line.

Near-post meniscus-induced migration and assembly of bubblesJianlin Liu ^{a, *}, Shanpeng Li ^b, Jian Hou ^{b, c, *}

^a *College of Pipeline and Civil Engineering, China University of Petroleum, Qingdao
266580, China*

^b *College of Petroleum Engineering, China University of Petroleum, Qingdao 266580,
China*

^c *State Key Laboratory of Heavy Oil Processing, China University of Petroleum,
Qingdao, 266580, China*

* Corresponding author: Jianlin Liu, E-mail: liujianlin@upc.edu.cn. Jian Hou, E-mail: hujian@upc.edu.cn.

Abstract

Although the effect of interfacial tension of liquid is often negligible at macroscale, it plays an essential role in such areas as superhydrophobicity on rough surfaces, water walking of aquatic creatures and self-assembly of small particles or droplets. In this study, we investigate the migration and assembly of bubbles near the meniscus produced by a slender post with various cross sections. The results show that the bubble always migrates to the solid wall of the post, although the cross section shape, material and tilt angle of the post are different. Especially, the final position of the bubble is not located at the singular point of the cross section, which is beyond what we have imagined. We simulate the morphology of the triple contact line via Surface Evolver, and then address the mechanism of bubble's migration from the viewpoint of force analysis and energy calculation. The factors governing the final position of the bubble are analyzed according to the scaling law. These obtained results cast new light on modulating the assembly of bubbles and small droplets by varying the material, geometric shape and posture of the post in water. These findings also have important implications for oil collection and oil displacement in petroleum engineering, drug delivery, design of microfluidic devices and chemical sensors.

Key words:

Meniscus; bubble migration; post standing in water; interfacial tension; principle of least potential energy

1. Introduction

Although the magnitude of interfacial tension of liquid is weak and even negligible at macroscale, it is accompanied with a plethora of interesting phenomena in nature and industry. For example, some plants' leaves can strongly repel water and dust [1]; aquatic insects can walk freely on water [2]; Texas horned lizards can drink water from mud via capillary channels [3]; droplets impact and bounce on surfaces like balloons [4, 5]; spider webs can transport and collect water [6]. In the spirit of learning from nature, various ultrahydrophobic surfaces, microfluidic devices, biomimetic robots have been engineered and put into use [7–9].

Another property of surface tension is that it can cause the spontaneous motion of droplets, particles and living creatures, in the absence of electric or magnetic fields. The most typical example is that a droplet can be propelled directionally in some particularly designed geometric structures, especially when the drop is bounded by two nonparallel surfaces [10], impaled by a conical fiber or on its surface [11, 12], and located in a conical tube [13]. One explanation is that the curvature of the special structure can create a “virtual” driving force to push forward these droplets [14]. Besides the geometric structures, a droplet placed on a substrate with heterogeneous interfacial energies can move towards the more hydrophilic area. In particular, an intriguing fact is that a droplet can even climb up to the top of an oblique substrate as the two ends of the surface have different wetting capabilities [15–17]. Additionally, small particles or flakes floating on the interface between two fluids can be self-assembled by the lateral component of the capillary force [18–23], which holds

great potential for mineral selection and emulsion production, etc. As a consequence, a number of studies, both in theoretical and experimental aspects, have been carried out on the migration of solid particles under the action of capillary forces, where the particles take various shapes, such as spheres, disks and cylinders [24–31]. Inspired by these facts, the meniscus near the solid wall can attract small insects or creatures from water to the bank automatically, which is crucial for their survival and reproduction [32].

It should be stressed that although much effect has been devoted on the meniscus-induced motion of small particles, it is rarely reported on the bubble or droplet migration near the meniscus. Vella and Mahadevan proposed that bubbles near the solid wall can adhere to the solid wall finally, due to the action of the two-dimensional meniscus [33]. More recently, Li et al. proposed that the meniscus near the planar solid wall repels the oil droplets, and can attract them after some surfactant is added in water [34]. However, there is hitherto an unknown on the migration of bubbles caused by a three-dimensional meniscus, for example, the one around a post standing in water, which is just the present task of this study. It sounds that the current problem is not trivial, but more complex and challenging, as the meniscus shape is governed by the principal curvatures in two directions, or the so-called Gaussian curvature and average curvature instead. This topic actually is a fundamental subject for bubble fractionation in chemical engineering [35], the oil displacement in the steam-foam process [36] and collection of oils from emulsified oil wastes in petroleum engineering [37]. Therefore, our motivation is directed to

examine how and why bubbles migrate and assemble near the post-induced meniscus. The goal of the study is to gain a full insight of the mechanics behavior of the bubble-meniscus interplay, and to provide some inspirations for engineering applications.

The outline of this article is organized as follows: In Section 2, we briefly introduce the experimental setup. In Section 3, we concentrate on the motion behavior of bubbles near the meniscus around a post with various cross sections. In succession, the force analysis and energy calculation are both performed to uncover the mechanism of bubble's movement, and the morphology of the triple contact line is simulated. In Section 4, we first discuss the physical parameters determining the final position of the bubble. Next, we explore the migration of a bubble near a tilted post, and then point out the potential applications of bubble migration and assembly. Finally conclusions are reached.

2. Experimental setup

A cuboid glass vessel with the volume of $12 \times 10 \times 12 \text{ cm}^3$ is used, which is placed horizontally on the test bed in our lab, and this setup ensures the water inside it takes on a horizontal surface. The ambient temperature in the room is roughly 25°C , and the adopted water is the normally used drinking water. In the experiments, a slender post is inserted into water vertically, which induces an obvious meniscus arising around it. The span length of the meniscus is within the range of capillary length $\kappa^{-1} = \sqrt{\gamma/(\rho g)} \approx 2.71 \text{ mm}$, where the surface tension of water $\gamma = 72 \text{ mN/m}$,

mass density of water $\rho=1.0 \text{ g/cm}^3$, and g is the gravitational acceleration.

The sample posts which take the circular, elliptic, square, rectangular, equilateral triangular, isosceles triangular, regular pentagonal and regular hexagonal cross sections are respectively investigated. Most of the posts are made of organic glass, and some of them are made of plastic for comparison. As most of the materials in our daily life are not hydrophobic, herein, we are only concerned with the hydrophilic posts. The Young's contact angle of a water droplet on the organic glass is measured as $\theta_Y = 53.5^\circ$, via a contact angle goniometer (Biolin Scientific Corporation, Thetalit 100). The Young's contact angles of a droplet on two types of plastics used in the experiment are also measured by the goniometer, with the values of 57.7° and 66.2° , respectively.

Near the meniscus around the post, a bubble is released on the water surface, with a distance of about 1 cm away from the post. The morphology of the liquid-liquid and liquid-vapor interfaces, the shape of the triple contact line around the post, and the trajectory of the bubble are all recorded by a camera (Canon SX240HS), whose effective pixel is 12,100,000.

3. Experiments and simulations

3.1 Post with a circular cross section

We first consider a post made of organic glass with a circular cross section, whose radius is 4 mm. When it is vertically standing in water, an axisymmetrical meniscus is formed around the solid wall. A bubble with the volume of 50 mm^3 is

deposited near the meniscus, which is created by an injector for medical purpose with the volume of 25 ml. For a spherical bubble, we have the scaling relations as follows:

The surface energy

$$W \propto \gamma S, \quad (1)$$

and the gravity

$$G \propto \rho g S \delta, \quad (2)$$

where ρ is the density of water, S is the surface area and δ is the thickness of the bubble film. As a consequence, a non-dimensional parameter, i.e. surface-gravity ratio

$$P = \kappa W / G \propto \frac{d}{\delta \sqrt{Bo}} \quad (3)$$

is introduced, which represents the competition between the surface energy and gravity of bubble. The symbol $Bo = \frac{\rho g d^2}{\gamma}$ is the Bond number, where d is the characteristic diameter and δ is the thickness of the bubble. Notice that the value of the Bond number is close to 1 in the current experiment, and $d \gg \delta$, then a reasonable postulation is that the gravity of the bubble can be neglected throughout the entire study.

It is observed that the bubble moves quickly towards the post, finally attaches to its solid surface after 4.5 s, as shown in the snapshots of Fig. 1(a). In fact, the similar phenomenon were also noticed by Vella *et al.* [33] and Li *et al.* [34], where a bubble can climb a meniscus between a planar solid wall and the horizontal water surface. The curve about the distance of the bubble head to the post wall x versus the passed time t is plotted in Fig. 1(b). The arrow indicates the time t_{\max} when the bubble

attaches to the post wall, with the value of 4.5 s for the post with a circular cross section. In the set of Fig. 1(b), the $\log(x)$ versus $\log(t_{\max}-t)$ diagram implies that the trajectory of bubble can be expressed by a power law function

$$x \propto (t_{\max} - t)^\eta, \quad (4)$$

and then the velocity of the bubble is derived as

$$v \propto \eta (t_{\max} - t)^{\eta-1}, \quad (5)$$

where the parameter is fitted as $\eta=0.33$. Furthermore, inserting Eq. (4) into (5) yields

$$v \propto \eta x^{1-1/\eta}, \quad (6)$$

and the function curve of v versus x is depicted in Fig. 1(c). These power law relations are similar to those of colloid particle interaction, which can also be analyzed from the interaction potential [28].

The secret of the bubble migration can be uncovered straightforward from the viewpoint of force analysis. As observed in the experiment, the bubble distorts the shape of the liquid-vapor interface of the meniscus, which is shown in Fig. 1(a). At the triple contact line, the bubble satisfies the famous Neumann's boundary condition, where the three interfacial tensions have fixed angles. As schematized in Fig. 2(a), a two-dimensional bubble is lying on the meniscus, where the surface tensions ahead and after the bubble present certain angles with the horizontal surfaces α and β , respectively. Then the Newton's second law leads to

$$ma = \gamma(\cos \alpha - \cos \beta) - c\mu v, \quad (7)$$

where m is the mass, a is the acceleration of the bubble, μ is the viscosity of water, and c is a coefficient correlated with the shape of the bubble [28]. It can be seen that if

$\alpha < \beta$, then the bubble can move towards the solid post. The scaling law is: $v \ll \text{cm/s}$, $d \ll \text{mm}$, $\mu \ll \text{mPa}\cdot\text{s}$, therefore the value of $Re = \frac{\rho v d}{\mu}$ is scaled as 1. In the motion, the acceleration term on the left side can't be neglected and the hydrodynamic resistance of the bubble really takes effect.

The difficulty of the force analysis is that the shape of the bubble changes at any moment when it moves to the post, and it is intractable to get the exact solution of the problem. Therefore, in order to demonstrate a clearer physical scenario, we will give the energy cascade of the whole system during the bubble movement. First it is necessary to extend our understanding on the meniscus morphology in space, which is governed by the famous Young-Laplace equation

$$\nabla \cdot \mathbf{n} = \kappa^2 z, \quad (8)$$

where \mathbf{n} is the unit outward normal of the meniscus surface, $\kappa^2 = \rho g / \gamma$, and z is the height of any point in the liquid/vapor interface above the horizontal water surface. In particular, for the axisymmetrical case, i.e. before the bubble is deposited, the Young-Laplace equation can be recast in the cylindrical coordinate system $O-rz$

$$\frac{1}{(r + r_0)\sqrt{1 + \dot{r}^2}} - \frac{\ddot{r}}{(1 + \dot{r}^2)^{3/2}} = -\kappa^2 z, \quad (9)$$

where r_0 is the radius of the circular cross section, O is the circle center, and the dot over a character represents the derivative with respect to z . The boundary conditions are then prescribed as $r=r_0$, $\dot{r} = -\cot \theta_y$; $r \rightarrow \infty$, $\dot{r} \rightarrow \infty$, $z=0$. The Laplace equation (9) can be numerically solved, and then the ground free energy of the whole system can be obtained. However, when a bubble is placed on the meniscus, it creates a

monopole at the interface, which has a larger surface area than the undisturbed interface, and its morphology is displayed in Fig. 2(b) via the online free software Surface Evolver [38]. Since the solid wall is hydrophilic and after the bubble is deposited, the triple contact line of the post is not a planar curve, where the points in this curve have different heights, that is to say, the curvature of the triple contact lines around the post and the bubble are different for each point. The post has deformed the liquid-vapor interface, whose average curvature decays with the distance decreasing. It can be seen that the profiles of the bubble and the triple contact lines around the post and the bubble are in agreement with the experimental results of Fig. 1(a). It is just the interaction between these curvatures that drives the migration of the bubble.

It has been proposed that the main driving force for the particle migration on the interface is the propensity for the interface to reduce the total excess surface area created by the presence of the particle [23]. Similarly, an energy approach is adopted here to explore the mechanism of the bubble migration, and due to the complexity of the system, we won't concentrate on the first principle analysis on the energy expressions, but utilize a numerical scheme via Surface Evolver. When a bubble is placed on the meniscus, the current free energy of the system can be expressed as

$$U_T = U_{B1}^{LV} + U_{B2}^{LV} + U_M^{LV} + U_M^{SL} + U_M^G + U_B^G, \quad (10)$$

where U_{B1}^{LV} is the bubble-air interfacial energy of the bubble, U_{B2}^{LV} the bubble-liquid interfacial energy of the bubble, U_M^{LV} the liquid-vapor interfacial energy of the meniscus, U_M^{SL} the solid-liquid interfacial energy of the meniscus, and the last two terms U_M^G and U_B^G are the potential energies due to the gravity of the

lifted water of the meniscus and that of the bubble, respectively. In the modeling process, the morphology of the meniscus is first calculated by the software according to Eq. (8). The liquid-vapor interface is then discretized by the triangle elements by virtue of the interpolation skill. The calculation by Surface Evolver deals with the finite difference method and conjugate gradient algorithm, which are helpful to find the minimum value of the whole free energy. As shown in Fig. 2(b), the bubble's shape is always changing while it is moving, and this stresses that the bubble doesn't have a constant shape in the simulation process.

For simulation, the interfacial tension of the bubble is chosen as 144 mN/m in consideration of its double liquid-vapor interfaces. The dependence relationship between the energy variation of each term in Eq. (10) and the distance of the bubble head to the post wall x is depicted in Fig. 2(c), where L1, L2, L3, L4, L5, L6 correspond to U_M^{LV} , U_{B2}^{LV} , U_B^G , U_M^G , U_{B1}^{LV} , U_M^{SL} , respectively, and L7 represents the total free energy U_T of the system. The migration of bubble is governed by the competition between the interfacial energies and the gravitational potential energies. It can be seen that there are only two terms, i.e. the liquid-air interfacial energy and the liquid-bubble interfacial energy increasing, but the remaining terms all decreasing with the distance reducing. As a result, the total free energy of the system is the summation of all the terms, which decreases greatly when the bubble approaches the solid wall. Especially, when the bubble attaches to the wall, the system holds the lowest free energy. In the light of the principle of least potential energy, the bubble will always moves to the most favourite position, i.e. the post's side wall.

Moreover, the total free energy curve can be fitted as a power law relationship with the distance x , which is written as

$$U_T \propto x^\varphi, \quad (11)$$

where the parameter $\varphi = -1.15$. This power law relation in Eq. (11) also corroborates the previous result on the particle interaction [28]. As a consequence, the driving force for the bubble can be deduced as the derivative of the free energy:

$$F_{driv} = -\frac{dU_T}{dx}. \quad (12)$$

Evidently, the physical meaning on the slope of the energy curve represents the value of the driving force. As displayed in Fig. 2(c), the nearer of the bubble to the post wall, the bigger of the driving force's value, and the bubble moves faster. In a word, the acceleration of the bubble is governed by the energy gradient of the system. This feature is also in agreement with the observation in the experiment.

3.2 Post with an elliptical cross section

For a post with an elliptical cross section inserted in water, there appears an anisotropic meniscus around it. When a bubble is placed near the meniscus, it finally adheres to the post wall in 4.5 s, as shown in Fig. 3(a). However, opposite to the reported result [24] that rod-like particles move to the position where the ellipse itself has the highest curvature, i.e. point A in the inset of Fig. 3(b), the bubble always comes to the point with lowest curvature on the elliptical curve, i.e. point B.

This abnormal phenomenon can be addressed by noticing that the two models are different. In the previous study, the triple contact line around the elliptical

cross-sectional post keeps a planar curve, perpendicular to the post's axis. This is mainly attributed to the fact that the triple phase contact line is pinned at the corner of the post [24]. In this planar curve, i.e. the ellipse, point A is of the highest curvature, and point B of the lowest curvature. Yet in the current experiment, it is observed that the triple contact line forms a more complicated closed curve in space, which is highest at point B and lowest at point A, as shown in the two side views of Fig. 3(b). The rough judgment is that the buoyancy of water will push the bubble to the highest point, where it is in an energetically favorable and thermodynamically stable state.

In order to further rationalize this phenomenon, we perform the simulation in use of Surface Evolver. The material of the post is organic glass, and the longer and shorter axes of the ellipse are 6 and 2 mm, respectively. We imagine a trajectory of the bubble approaching to point A along the longer axial direction of the ellipse, as schematized in the left inset of Fig. 3(c). The energy curve indicates that the bubble will adhere to point A with x (the distance to point A) decreasing, as the system has lower free energy in this motion trail. Similarly, in the second trajectory, if the bubble moves in the direction of the shorter axis of the ellipse (shown in the right inset of Fig. 3(c)), it finally stops at point B as the system is of the lowest free energy. Clearly, the free energy of the system has a much lower value at point B than that at point A. This result presents a reasonable explanation of the bubble's final position around an elliptical cross-sectional post.

3.3 Post with a rectangular cross section

As is well known, the circular and elliptical curves are both smooth at any point, but the rectangle has singular points at its sharp corners. Next we investigate the migration behavior of a bubble released near the meniscus induced by a post with a rectangular cross section, which is made of organic glass. It is found that the bubble finally stays at the midpoint of the longer side edge, even if it maybe first contacts with the shorter side of the post, as shown in Fig. 4(a). We have also changed the material of the post to two types of plastics, with the Young's contact angle $\theta_Y = 57.7^\circ$ and 66.2° , respectively. The same phenomena are observed for the plastic regular hexagon pillar, i.e., the bubble finally comes to the midpoint of the side edge. It implies that the property of material is not the key factor in deciding the motion direction and target of the bubble.

The reason for bubble's final position also lies in that the post produces an anisotropic meniscus, and the triple contact line surrounding the post takes a complicated morphology. As observed in the left sub-figure of Fig. 4(b), the triple contact line around a square ($4 \times 4 \text{ mm}^2$) has a lowest point at the corner, and those on the side surface are higher than this point. The distribution of the triple contact line is also simulated by the software of Surface Evolver, which is in excellent agreement with the experimental observation, as shown in the right sub-figure of Fig. 4(b).

The phenomenon can also be accounted for by the principle of energy minimization, which is realized by the simulation of Surface Evolver. The two side lengths for the rectangular cross section of the post are 2 and 8 mm, respectively. In the triple contact line, the lowest points are at the corners and the highest points are

located at the midpoints of the longer side edges. If the short side length is fixed at 2 mm, and with the increase of the longer side length, the heights (H) of the midpoints in the short side and long side both increase, as shown in Fig. 4(c). The length ratio is defined as $r=a/b$, where a and b are the lengths of the long side and short side, respectively. In the infinite case, the post is close to a plate standing in water, and the heights attain to definite values. The aforementioned experience tells us that the bubble will stay at the highest positions of the meniscus, and it indicates that the cross section shape of the post can be reasonably designed to regulate the position of the bubbles or small droplets.

We select three trajectories as schematized in the three insets (top view) of Fig. 4(d): (1) The straight line from the bubble head to the midpoint of the short side; (2) The straight line to one corner; (3) The straight line to the middle of the long side. The simulation result shows that in the third route, the system can finally arrive at a state with minimum free energy, as displayed in Fig. 4(d). The second curve is between the first and third curves, and this manifests that when the bubble stays at the midpoint of the short side edge, it is in an energetic metastable state. With the small perturbation, the bubble will jump from this point to the most stable position, i.e. to the midpoint of the longer side edge.

4. Discussions

4.1 Parameters governing the bubble position

For the normal geometric elements considered, including circle, ellipse,

equilateral triangle, isosceles triangle, rectangle, square, regular pentagon, and regular hexagon, they can be grouped into two types: smooth curves and polygons with singular points. The number of the singular points is denoted by N , then $N=0, 1, 2, 3, 4, 5$ and 6 for the above geometric elements. We also introduce an asymmetric factor

$$R=a/b. \quad (13)$$

For the ellipse, a and b are the lengths of the longer axis and shorter axis, respectively. Especially for the circle, $R=1$. For the polygons, a and b are two representative side lengths. For instance, for the equilateral triangle, square, regular pentagon and regular hexagon, $R=1$; for the isosceles triangle and rectangle, $R>1$. It should be noted that for the rectangle, the parameter R is just the symbol r defined in Section 3.3. The phase diagram about R and N is depicted in Fig. 5.

For the post cross section with the above mentioned polygonal shapes, the meniscus-induced bubble migration phenomena are all analyzed. It is found that the bubble always moves to the midpoints of the longest side edge, as the triple contact line has the highest point. It can be judged that the final height of the bubble is determined by the surface tension and density of the liquid, the parameters R and N , the characteristic length l of the post (such as the side length or radius of the cross section), and the Young's contact angle θ_Y , which is scaled as

$$h = h(\gamma, \rho, R, N, l, \theta_Y). \quad (14)$$

As a result, the non-dimensional height is given as

$$\tilde{h} = \kappa^2 h l = \tilde{h}(R, N, \theta_Y). \quad (15)$$

It is seen that the dimensionless height is only correlated with the cross section shape

and the wetting property of the post, which paves a convenient way to control the position of the bubble or droplet.

4.2 Post tilted in water

In practice, it is easy to drive the bubble by altering the tilted angle of post. In what follows, we examine the motion of a bubble near an oblique post in water. The parameters of the post are the same as those in Section 3.1. As shown in Fig. 6(a), when the tilt angle is $\theta_t = 45^\circ$, the triple contact line forms an asymmetric curve in space, with different heights at different points. It manifests that on the left side of the post the triple contact line is lower, and on the right side it is higher. In a word, when the post is oblique, the bubble finally migrates to the corner of the post, staying at the area whose triple contact line is highest.

This process is also simulated in use of Surface Evolver, where three positions and trajectories are schematized in the insets of Fig. 6(b). The free energy curves of the system along the three trajectories are demonstrated in Fig. 6(b), which can expound that the bubble comes to the corner of the system. This fact provides insight into the mechanism and a straightforward strategy that by simply varying the posture of the post, one can modulate the bubble's assembly, besides its material properties and geometric shapes.

4.2 Potential applications

Moreover, bubbles can be self-assembled by polygonal cross-section with

multiple sides, forming a beautiful and ordered pattern. As shown in the left sub-figure of Fig. 7, six bubbles are contacting with the six sides of the hexagon (the side length is 8 mm) about the organic glass post, and a flower-like picture is emerging. The experiment is consistent with the numerical simulation via Surface Evolver, as shown in the right sub-figure of Fig. 7.

The attraction of bubbles to the side edges of a post with a polygonal cross section sheds new light on the collection of oils from emulsified oil wastes and oil displacement in the steam-foam technology in petroleum engineering, and assembly of small droplets on the interface. For instance, the bubble flotation technique is useful to collect oils, which gets increasing concerns for its high throughput and efficiency of the treatment of aqueous or oily effluents [37]; and the control of bubble migration and assembly paves a new way for the invention of flotation devices. In the steam-foam process, the high-permeability pores with heterogeneous curvatures are plugged by the input bubbles so that the steam can be diverted into the less-permeable layer to enhance recovery in petroleum engineering [36].

Another direct application of bubble migration is that it can be used to enrich metal ions from homogeneous solutions in mineral engineering or drug delivery. With the aid of interfacial adsorption, the bubble can play the role of a small collector and thus the extraction of metal ions can be naturally realized [35]. The biggest advantage of this bubble fractionation process is that there is no need to apply electric field, magnetic field, optical or acoustic field, etc.

4. Conclusions

In conclusion, the migration and assembly of bubbles near the meniscus induced by a slender post are comprehensively studied. The posts with circular, elliptical, square, rectangular, equilateral triangular, isosceles triangular, regular pentagonal and regular hexagonal cross sections are systematically analyzed. The results show that the bubble always migrates to the solid wall of the post, regardless of its cross section shape, material and tilted angle. It is also found that the bubble tends to stay at the point where the triple contact line is highest. The simulated morphology of the triple contact line is a complex curve in space, which validates the experimental observation. The force analysis and energy calculation are both conducted, which can address the motion behavior of the bubble according to the principle of least potential energy.

However, the detailed force analysis should be further carried out in future, where the Navier-Stokes equation with capillary effect is considered. In addition, the behavior of a bubble near a meniscus induced by a hydrophobic post is necessary to be explored in the following work. These analyses open a new venue to modulate the assembly of bubbles and small droplets by varying the material, geometric shape and posture in water. The obtained results hold great applications in oil collection from emulsified oil wastes and oil displacement in the steam-foam process in petroleum engineering, the extraction of metal ions in mineral engineering or drug delivery and the design of microfluidic devices.

Acknowledgement

This project was supported by the National Natural Science Foundation of China (11272357), and the Natural Science Fund for Distinguished Young Scholar of Shandong Province (JQ201302 and JQ201115), the Program for New Century Excellent Talents in University (NCET-11-0734) and the Fundamental Research Funds for the Central Universities (15CX08004A).

References:

1. W. Barthlott and C. Neinhuis, *Planta*, 1997, **202**, 1–8.
2. D. L. Hu, B. Chan and J. W. M. Bush, *Nature*, 2004, **424**, 663–666.
3. E. Grossman, *Nat. Wildlife*, 2004, **42**, 52–56.
4. D. Y. Zang, X. L. Wang, X. G. Geng and Y. M. Chen, *Soft Matter*, 2013, **9**, 394–400.
5. Y. Liu, L. Moevius, X. Xu, T. Qian, J. M. Yeomans and Z. Wang, *Nat.Phys.*, 2014, **10**, 515-519.
6. Y. Zheng, H. Bai, Z. Huang, X. Tian, F. Q. Nie, Y. Zhao, J. Zhai and L. Jiang, *Nature*, 2010, **463**, 640–643.
7. X. B. Zhang, J. Zhao, Q. Zhu, N. Chen, M. Zhang and Q. Pan, *ACS Appl. Mater. Interf.*, 2011, **3**, 2630–2636.
8. S. H. Hsu and W. M. Sigmund, *Langmuir*, 2010, **26**, 1504–1506.
9. R. Blossey, *Nat. Mater.*, 2003, **2**, 301–306.
10. F. Hauksbee, *Philos. Trans. R. Soc. London Ser. A*, 1712, **27**, 395–396.
11. E. Lorenceau and D. Quere, *J Fluid Mech.*, 2004, **510**, 29–45.
12. C. J. Lv, C. Chen, Y. C. Chuang, F. G. Tseng, Y. J. Yin, F. Grey and Q. S. Zheng, *Phys.Rev. Lett.*, 2014, **113**, 026101.
13. J. L. Liu, R. Xia, B. W. Li and X. Q. Feng, *Chin. Phys. Lett.*, 2007, **24**, 3210–3213.
14. Y. J. Yin, C. Chen, C. J. Lu and Q. S. Zheng, *Appl. Math. Mech.-Engl.*, 2011, **32**, 533–550.

15. J. Bico and D. Quéré, *J Fluid Mech.*, 2002, **467**, 101–127.
16. M. K. Chaudhury and G. M. Whitesides, *Science*, 1992, **256**, 1539–1541.
17. M. M. Weislogel, *AIChE J.*, 1997, **43**, 645–654.
18. G. M. Whitesides and B. Grzybowski, *Science*, 2002, **295**, 2418–2421.
19. D. Y. C. Chan, J. D. J. Henry and L. R. White, *J. Coll. Interf. Sci.*, 1981, **79**, 410–418.
20. M. Nicolson, *Proc. Cambr. Phil. Soc.*, 1949, **45**, 288–295.
21. S. Dasgupta, M. Katava, M. Faraj, T. Auth and G. Gompper, *Langmuir*, 2014, **30**, 11873–11882.
22. Y. Yu, M. Guo, X. D. Li and Q. S. Zheng, *Langmuir*, 2007, **23**, 10546–10550.
23. D. Stamou, C. Duschl and D. Johannsmann, *Phys. Rev. E.*, 2000, **62**, 5263–5272.
24. M. Cavallaro, L. Botto, E. P. Lewandowski, M. Wang and K. J. Stebe, *Proc. Natl. Acad. Sci.*, 2011, **52**, 20923–20928.
25. L. Yao, N. Sharifi-Mood, I. B. Liu and K. J. Stebe, *J. Colloid Interface Sci.*, 2015, **449**, 436–442.
26. N. Sharifi-Mood, I. B. Liu and K. J. Stebe, *Soft Matter*, 2015, **11**, 6768–6779.
27. K. McEnnis, A. D. Dinsmore and T. P. Russell, *Langmuir*, 2015, **31**, 5299–5305.
28. J. C. Loudet, A. M. Alsayed, J. Zhang and A. G. Yodh, *Phys. Rev. Lett.*, 2005, **94**, 018301.
29. C. Blanc, D. Fedorenko, M. Gross, M. In, M. Abkarian, M. A. Gharbi, J. B. Fournier, P. Galatola and M. Nobili, *Phys. Rev. Lett.*, 2013, **111**, 058302.
30. C. Zeng, F. Brau, B. Davidovitch and A. D. Dinsmore, *Soft Matter*, 2012, **8**,

8582–8594.

31. A. Würger, *Phys. Rev. E*, 2006, **74**, 041402.

32. D. Hu and J. W. M. Bush, *Nature*, 2005, **437**, 733–736.

33. D. Vella and L. Mahadevan, *Am. J. Phys.*, 2005, **73**, 817–825.

34. S. P. Li, J. L. Liu, J. Hou and G. F. Zhang, *Coll.Surf. A*, 2015, **469**, 252–255.

35. W. Walkowiak, *Sep. Sci. Technol.* 1991, **26**, 559–568.

36. G. J. Hiraski, *J. Petro. Technol.*, 1989, **41**, 449–456.

37. J. Rubio, M. L. Souza, R. W. Smith, *Miner. Eng.*, 2002, **15**, 139–155.

38. K. A. Brakke, *Exp. Math.*, 1992, **1**, 141–165.

Figure Captions

Fig. 1 (a) A bubble near the meniscus caused by a post with a circular cross section migrates to the side wall of the post. (b) The distance of the bubble head to the post wall x as a function of the time t . (c) The velocity of the bubble v as a function of the distance head to the post wall x .

Fig. 2 (a) Schematic of a bubble subjected to the interfacial tension difference at its head and tail. (b) Morphologies of the bubble and meniscus simulated by Surface Evolver in different position. (c) The energy curves with respect to the distance of the bubble head to the post wall, including all the energy terms (L1 to L6) and the total free energy (L7).

Fig. 3 (a) A bubble near the meniscus around a post with an elliptical cross section finally adheres to the post wall at a point where the ellipse has the smallest curvature. (b) Side view of the triple contact line around the post, where point A and B correspond to the points where the ellipse has the highest and lowest curvatures, respectively. (c) The total free energy curves of the system with respect to the distance of the bubble head to point A or point B along two trajectories, which are two straight lines (top view) linking the bubble head to point A and B, respectively.

Fig. 4 (a) A bubble near the meniscus migrates to the post with a rectangular cross section and adheres to the midpoint of the longer side edge. (b) Morphology of the triple contact line around the post with a square cross section, where the left figure is the experimental observation and the right is the simulation result. (c) The heights of the highest point of the triple contact line along the longer side and shorter side with

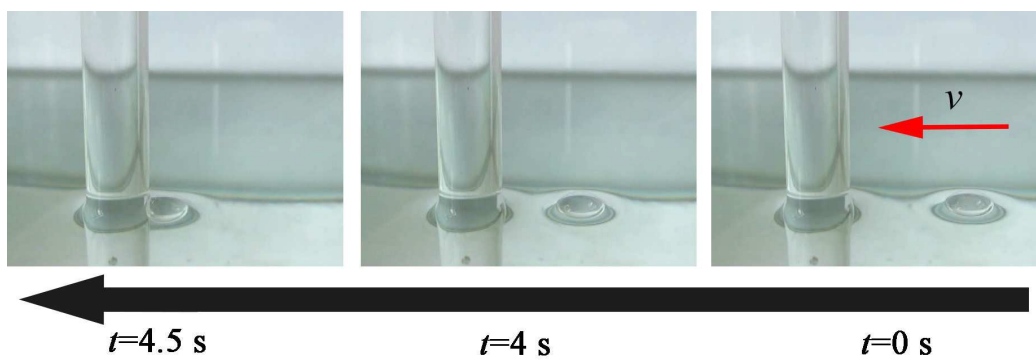
respect to the ratio of the longer side and the shorter one, where the inset shows the morphology of the triple contact line. (d) The total free energy curves of the system with respect to the distance of the bubble head to the post wall, where the three insets represent three trajectories of the bubbles. The trajectories are three straight lines (top view) linking the bubble head and the midpoints of the longer and shorter sides, and the corner.

Fig. 5 Two factors governing the cross-sectional morphology of a post, where N is the number of the singular points and R is the asymmetric factor.

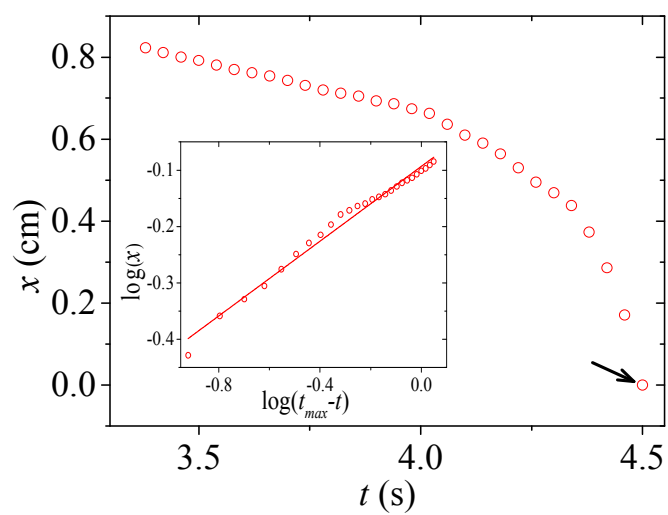
Fig. 6 (a) A bubble near the meniscus around a tilted post migrates to the position where the triple contact line is highest. (b) The total free energy curves of the system with respect to the distance of the bubble head to the post wall, where the insets stand for three positions and trajectories of the bubble.

Fig. 7 Six bubbles are assembled on the the six side edges of the post with a regular hexagonal cross section.

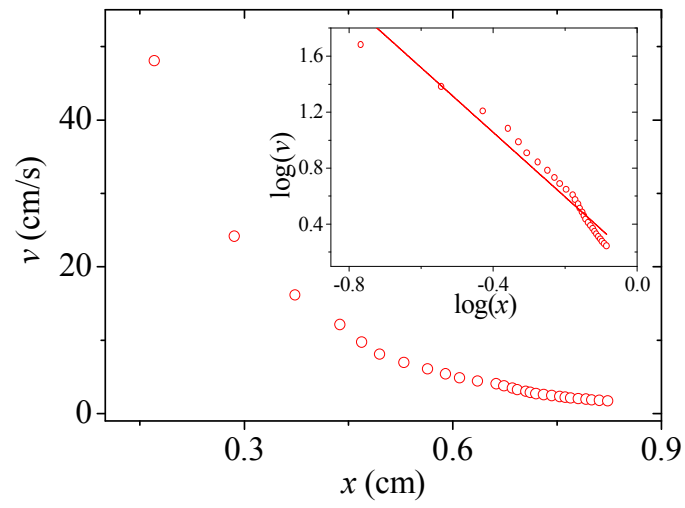
Figures



(a)

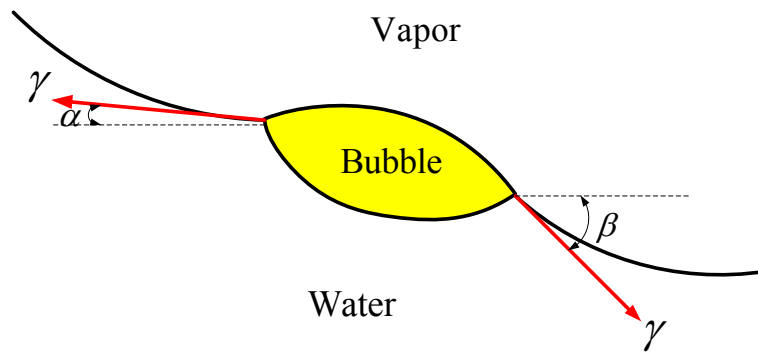


(b)

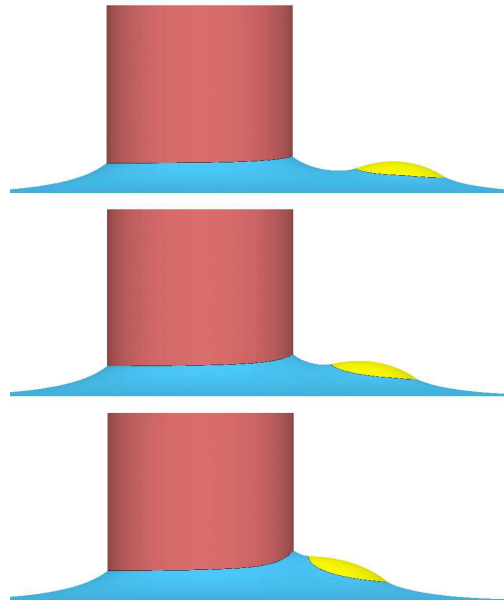


(c)

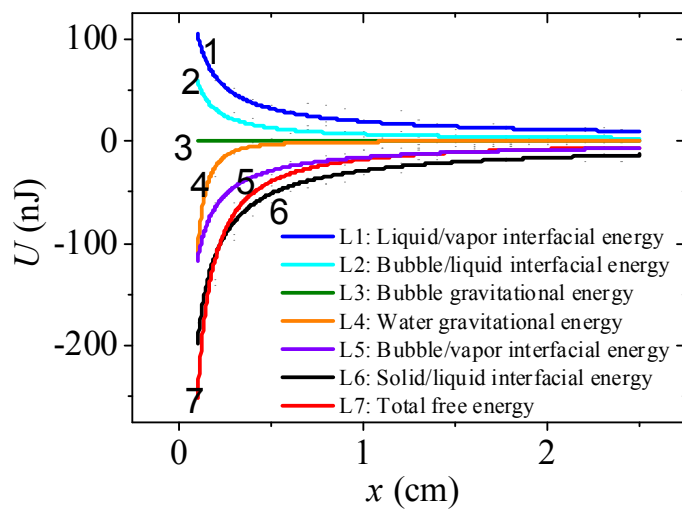
Fig. 1



(a)



(b)



(c)

Fig. 2

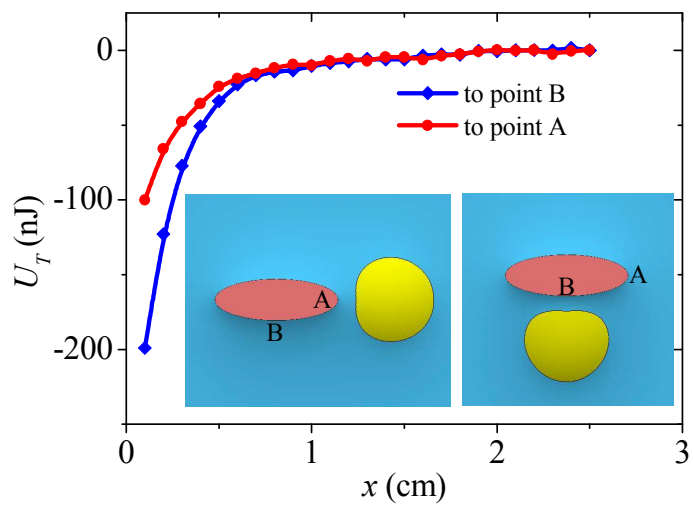
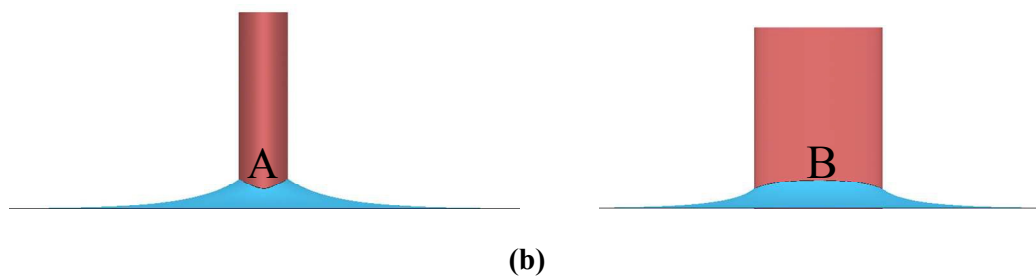
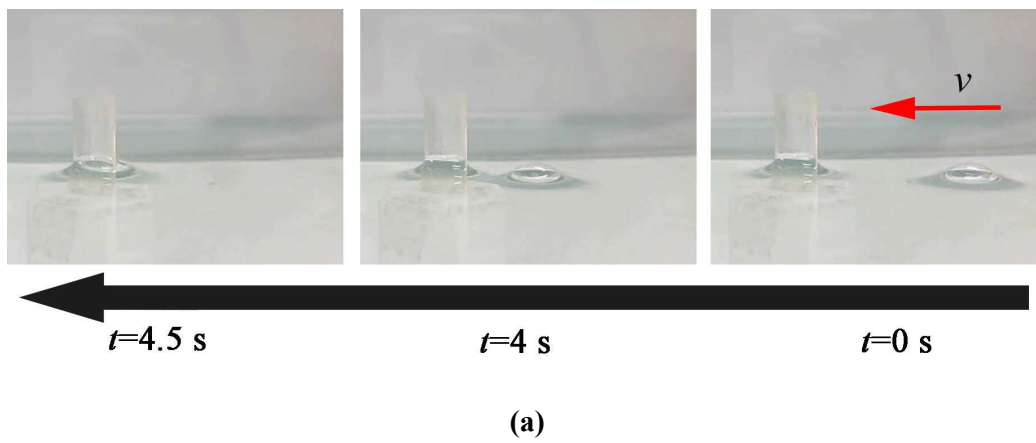
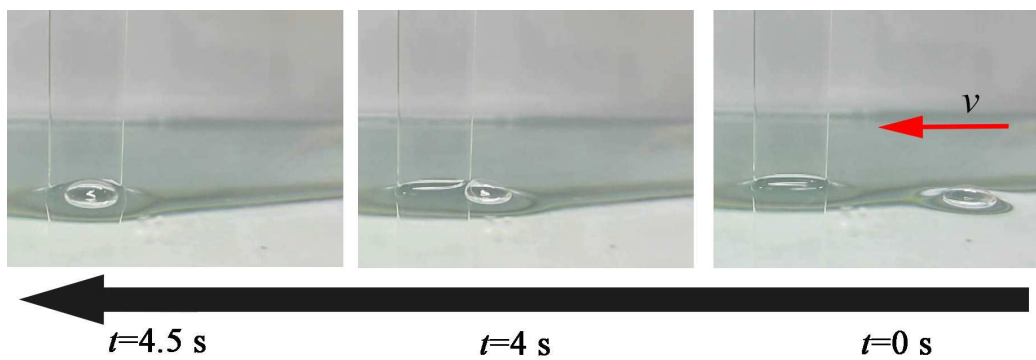
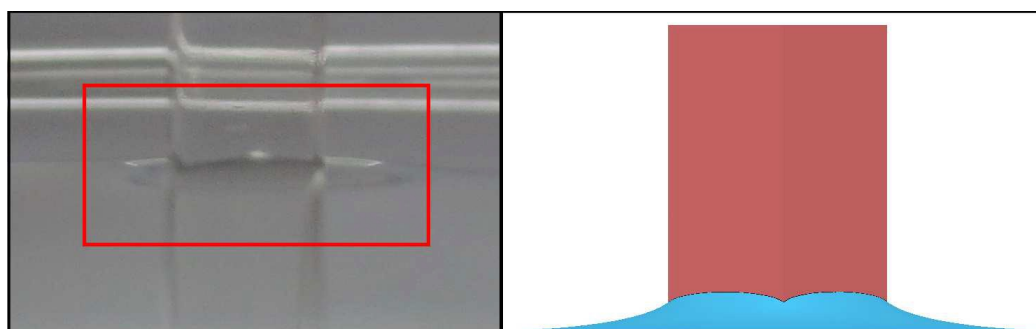


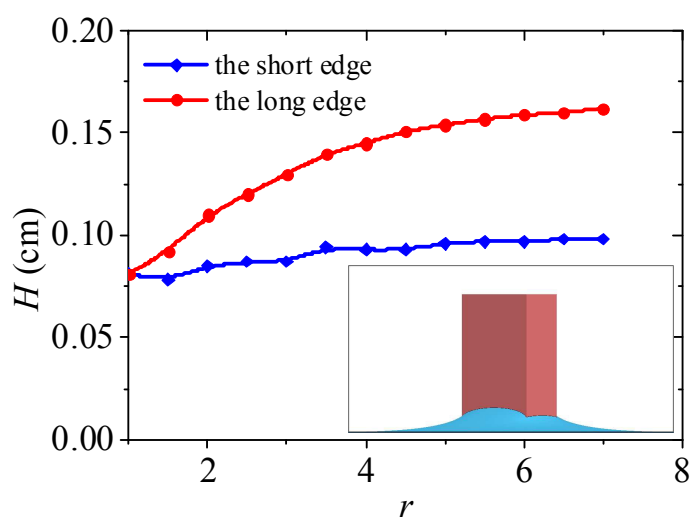
Fig. 3



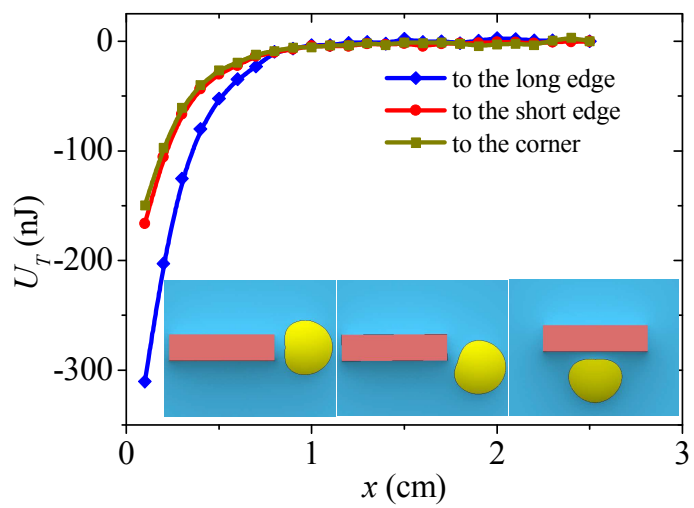
(a)



(b)



(c)



(d)

Fig. 4

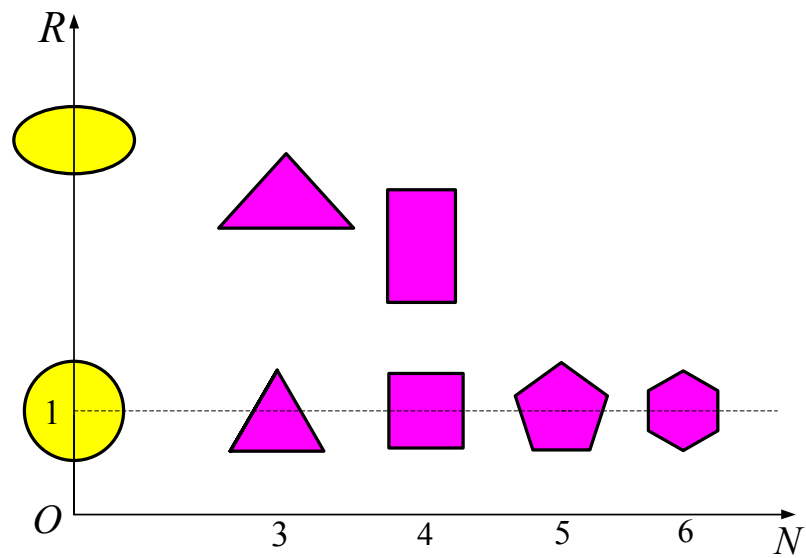
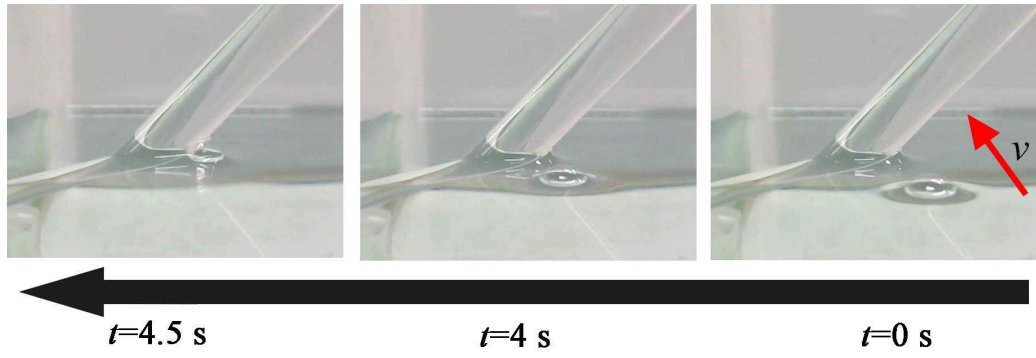
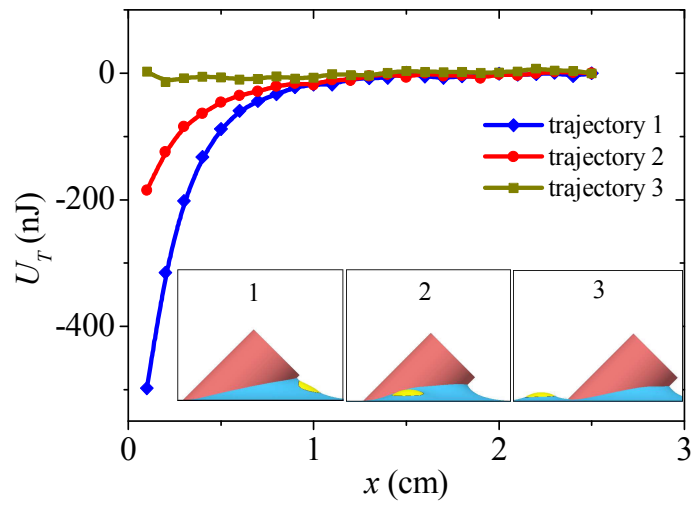


Fig. 5



(a)



(b)

Fig. 6

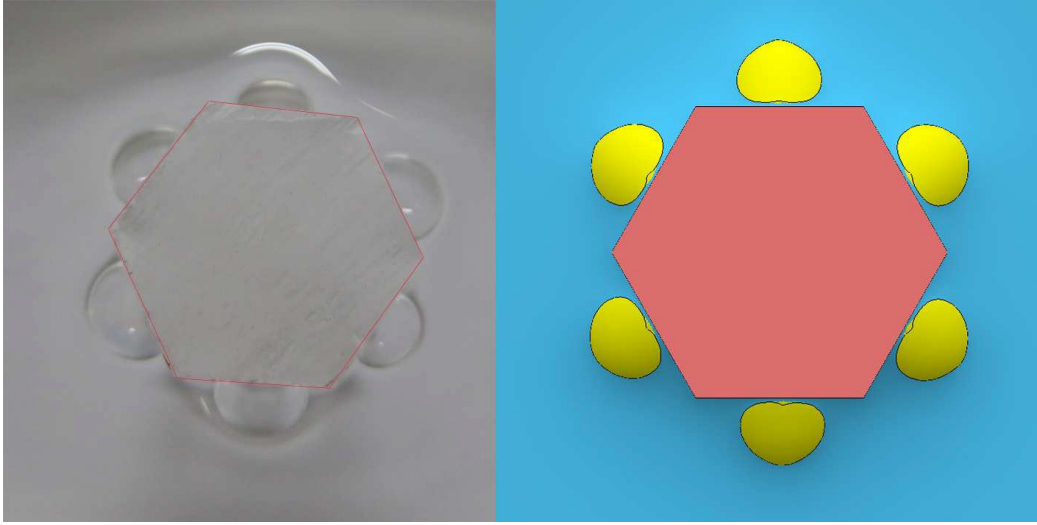


Fig. 7